Title
Search of Neutrinoless Double Beta Decay with the GERDA Experiment

Authors
Agostini, M
Allardt, M
Bakalyarov, AM
et al.

Publication Date
2016-04-01

DOI
10.1016/j.nuclphysbps.2015.09.303

Peer reviewed

Nuclear Instruments and Methods in Physics Research A 622 (2010) 97–106

Contents lists available at ScienceDirect

Nuclear Instruments and Methods in Physics Research A

journal homepage: www.elsevier.com/locate/nima

Commissioning of the HELIOS spectrometer

J.C. Lighthall [a,b,*], B.B. Back [b], S.I. Baker [b], S.J. Freeman [c], H.Y. Lee [b], B.P. Kay [b], S.T. Marley [a,b], K.E. Rehm [b], J.E. Rohrer [b], J.P. Schiffer [b], D.V. Shetty [a], A.W. Vann [b], J.R. Winkelbauer [a], A.H. Wuosmaa [a]

[a] Department of Physics, Western Michigan University, 1903 W. Michigan Ave., Kalamazoo, MI 49008-5252, USA
[b] Physics Division, Argonne National Laboratory, 9700 South Cass Ave., Argonne, IL 60439, USA
[c] Schuster Laboratory, University of Manchester, Brunswick Street, Manchester M13 9PL, UK

ARTICLE INFO

Article history:
Received 22 May 2010
Received in revised form
15 June 2010
Accepted 16 June 2010
Available online 25 June 2010

Keywords:
Spectrometer
Inverse kinematics
Transfer reactions
Solenoid

ABSTRACT

This paper describes the implementation and commissioning of a device based on a new concept for measurements of nuclear reactions in inverse kinematics. The HELIcal Orbit Spectrometer, HELIOS, was commissioned at Argonne National Laboratory by studying the ^{28}Si(d,p)^{29}Si reaction in inverse kinematics. This experiment served as a proof of principle for this previously untested concept, and was used to verify the response and performance characteristics of HELIOS.

1. Introduction

The worldwide development of radioactive ion beam facilities is permitting a new generation of nuclear reactions to be studied. Radioactive beams enable the study of nuclei having half-lives too short to make them suitable for targets. Reactions utilizing such exotic beams permit measurements of nuclear properties further away from stability than previously possible. The technical challenges of studying such reactions require new approaches for detecting the charged particles that are produced.

Quasi-elastic transfer reactions such as (d,p), (^{3}He,d), and (α,t) have traditionally been used to determine many nuclear properties. With stable isotopes, these studies were carried out by bombarding a heavy target with light beams of deuterons or helium isotopes [1]. With radioactive beams, however, the beam and target must be exchanged, with a heavy-ion beam bombarding a light target. In this regime of "inverse kinematics," the center of mass of the reaction has a substantial velocity in the laboratory frame. With light beams incident on a stable target, the velocity of the center of mass is small, while in inverse kinematics it is nearly that of the beam. Thus, the energies of the emitted light ions are highly angle-dependent and at backward angles ($\theta_{lab} > 90^\circ$) and the separation between excited states in the laboratory is less than that in the center of mass ("kinematic compression") [2]. For example, in the d(^{28}Si,p)^{29}Si reaction at a bombarding energy of 6 MeV/u, excited states separated by 1 MeV in the center of mass are separated by 440 keV in the laboratory for $\theta_{lab} = 170^\circ$. This effect of kinematic compression increases with the mass of the beam. Furthermore, due to the low energies of the light ions at backward angles, particle identification is difficult.

To address the resolution problems encountered in inverse kinematics, one approach is to implement a large, highly segmented detector array with excellent angle resolution. This method requires a complicated system of detectors and electronics. A common limitation of any standard approach is the difficulty in identifying the emitted light ion [2]. A different technique suggested by Refs. [3–5] eliminates kinematic compression and provides particle identification. The HELical Orbit Spectrometer (HELIOS) at Argonne National Laboratory is the first implementation of this concept.

This paper describes the results of a measurement used to commission HELIOS. As the approach was previously untested, the commissioning served as a proof of principle. The implementation of the HELIOS concept and its first application to the measurement of a nuclear reaction—neutron transfer with the ^{28}Si(d,p)^{29}Si reaction in inverse kinematics—are presented.

2. The HELIOS concept

The HELIOS concept is described in Ref. [5]. Briefly, HELIOS is based on a large-bore superconducting solenoid, as shown

* Corresponding author at: Department of Physics, Western Michigan University, 1903 W. Michigan Ave., Kalamazoo, MI 49008-5252, USA. Tel.: +1 630 252 4803.
E-mail address: jonathan.c.lighthall@wmich.edu (J.C. Lighthall).

0168-9002/$ - see front matter © 2010 Elsevier B.V. All rights reserved.
doi:10.1016/j.nima.2010.06.220

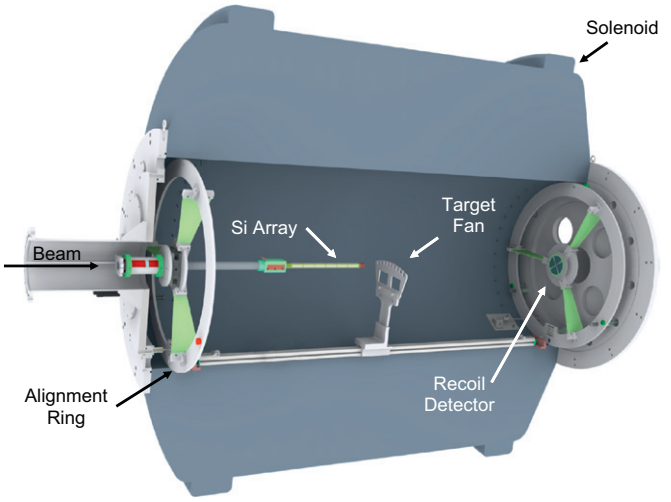

Fig. 1. Schematic view of the HELIOS spectrometer. The accelerated beam enters from the left. Shown are the silicon-detector array supported on the upstream alignment ring, and the rotating target fan. Also shown is a silicon-detector array for recoil detection which was not used in the present experiment.

schematically in Fig. 1. Beams enter the solenoid along the magnetic axis, passing through a hollow array of position-sensitive silicon detectors. The beam then intercepts a light target, also on the magnetic axis. Particles emitted at the target are transported in helical orbits back to the axis where they are detected in the silicon array. The forward-going heavy beam-like ions can also be detected in recoil detector at forward angles; such a detector was not implemented in the measurement described in this paper, but has been used in subsequent experiments [6].

In a uniform magnetic field $\mathcal{B}$, the time of flight of an ion of mass m and charge qe returning to the axis is equal to its cyclotron period $T_{cyc}=(2\pi/\mathcal{B})(m/qe)$, thus yielding determination of the mass-to-charge ratio m/q. This approach solves the problem of light charged particle identification at low energy. A measurement of the position where the particles return to the solenoid axis relative to the target (the return distance "z"), combined with the fixed time-of-flight, corresponds to dispersion according to the laboratory velocity parallel to the beam axis $v_{\|}=z/T_{cyc}$. In this mode, there is a linear relationship between position z, the particle energy in the laboratory E_{lab}, and the energy in the center-of-mass frame E_{cm}, as given by Eq. (5) of Ref. [5]:

$$E_{lab}=E_{cm}-\frac{1}{2}mV_{cm}^2+\left(\frac{mV_{cm}}{T_{cyc}}\right)z \tag{1}$$

where V_{cm} is the velocity of the center-of-mass frame in the laboratory.

This relationship between the laboratory quantities and those in the center-of-mass system is the key to the enhanced Q-value resolution of the HELIOS Spectrometer—the separation in laboratory energy between kinematic groups corresponding to different energy levels in the residual nucleus at a fixed z is equal to the spacing in the center-of-mass frame. In HELIOS, angle measurements in inverse kinematics are transformed into position measurements along the solenoid axis; such distance measurements can be made using position-sensitive detectors.

The relationship given in Eq. (1) is an idealization that assumes a detector array of zero radius, with the return distance z equal to its ideal value z_0. With a detector of non-zero radius, the return distance z does not equal z_0, but can still be calculated analytically. Fig. 2 shows an analytic calculation of proton energies and center-of-mass angles versus z for the d(^{28}Si,p)^{29}Si reaction at a bombarding energy of 6 MeV/u. The calculation

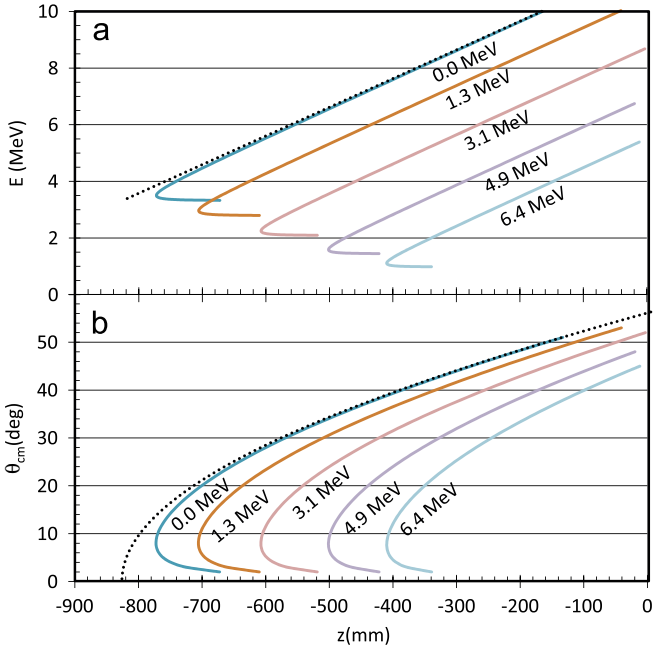

Fig. 2. Analytical calculation of laboratory energies and center-of-mass angles plotted versus return distance z for protons emitted from the d(^{28}Si,p)^{29}Si reaction corresponding to the population of various excited states in ^{29}Si. The target is placed at $z=0$ mm. The calculations assume a uniform, purely axial magnetic field, and a cylindrical detector of radius 11.4 mm. The dotted line in each plot corresponds to the ground-state transition as measured by a detector array of zero radius, illustrating the difference between the ideal return distance z_0 and the actual return distance to the detector z.

assumes a cylindrical detector array of radius $r_0=11.4$ mm and an ideal, uniform solenoidal magnetic field of 2.0 T. The actual proton return distance is given by

$$z=(v_0\cos(\theta_{cm})+V_{cm})\frac{r\left[2\pi-2\arcsin\left(\frac{r_0}{2r}\right)\right]}{v_0\sin(\theta_{cm})} \tag{2}$$

where v_0 is the particle velocity in the center-of-mass frame, V_{cm} is the velocity of the center-of-mass frame in the laboratory, r_0 is the detector radius, r is the radius of the cyclotron orbit, and θ_{cm} is the proton angle of emission in the center-of-mass frame. The effect of the finite radius of the detector, that $z\neq z_0$, becomes significant for protons emitted at very small angles relative to the solenoid axis and results in the "knees" seen in Fig. 2(a). For these angles the reduction in the transverse component of the particle's trajectory, by approximately r_0 from $2\pi r$, becomes significant and the approximate relationship between the detected position of the ions z and the axis intercept z_0 is given by

$$z\approx z_0-\frac{r_0}{\tan(\theta_{lab})}. \tag{3}$$

For most orbits, where the radius $r\gg r_0$, the effect of the non-zero size of the silicon-detector array is insignificant.

3. HELIOS technical description

3.1. The solenoid

The solenoid used in HELIOS is a superconducting magnet from a decommissioned Magnetic Resonance Imaging (MRI) device. The interior diameter of the solenoid bore is 92 cm and the length is 235 cm. The axial, radial, and azimuthal components of the magnetic field were measured using a three-axis Hall probe with the central magnetic field of the solenoid set to 2.0 T,

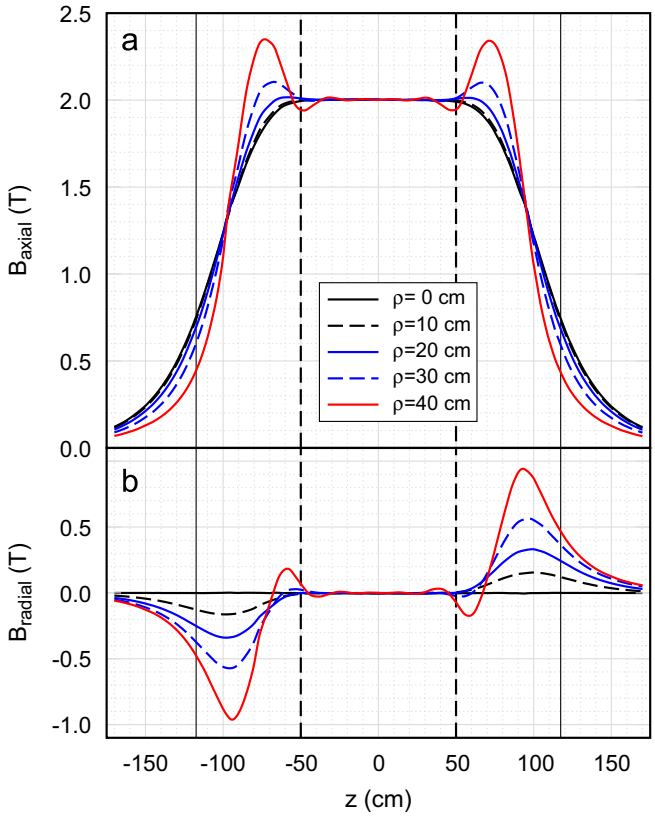

Fig. 3. Axial (a) and radial (b) components of the HELIOS magnetic field, as measured with the central field set to 2.0 T at several radial distances ρ from the solenoid axis. The vertical dashed lines indicate the region of highest field uniformity. The thin vertical solid lines denote the physical limit of the solenoid vessel.

although the maximum possible central field value is 2.86 T. The field was measured at 21,240 points inside and outside of the solenoid volume with an average spacing of approximately 4 cm between points. Fig. 3 shows the measured axial and radial field components at representative radial distances from the solenoid axis.

Within the precision of these measurements, the magnetic field is homogeneous and effectively purely axial to within 0.05% in a spherical region 90 cm in diameter about the geometric center of the solenoid. In terms of a volume relevant to particle trajectories, the maximum field deviation is less than 3% within a cylindrical region $z < \pm 50$ cm and $\rho < 40$ cm. As can be seen in Fig. 3, field deviations of this magnitude only occur at the edges of this region. On the solenoid axis, the axial field falls to 10% of its central value at $z \approx \pm 150$ cm from the center of the magnet and to 0.1% at $z \approx \pm 330$ cm from center. The radial field reaches a maximum absolute value of 63% of the central field at $z \approx \pm 95$ cm from the center of the magnet and at a radius of $\rho = 45$ cm. The azimuthal component of the magnetic field was found to be negligible throughout the magnet volume.

The solenoid was converted to a vacuum vessel by sealing the ends with aluminum flanges mounted to either end of the solenoid. Each flange features nine 4.45 cm diameter feed-throughs that are used to carry detector signals, cooling liquid, and other diagnostic signals from the inside of the magnet. An additional removable flange reduces the opening to mate with an 20 cm diameter beam pipe. A photograph of HELIOS as installed at the ATLAS facility at Argonne National Laboratory appears in Fig. 4.

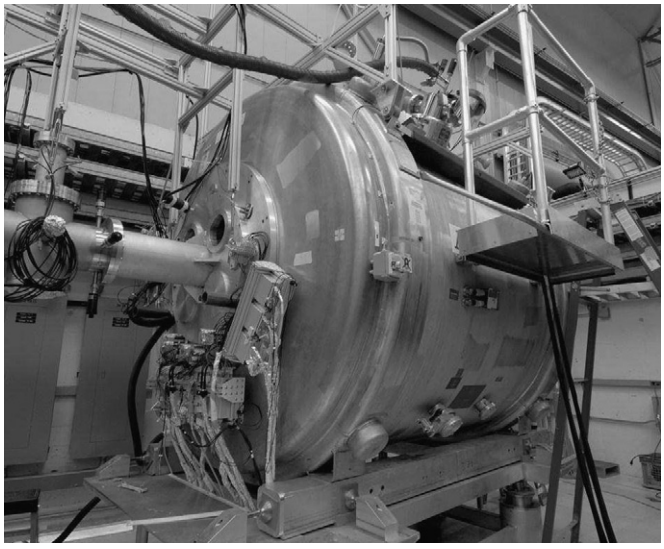

Fig. 4. The HELIOS spectrometer as installed at the ATLAS accelerator facility. Beam enters from left.

3.2. The silicon-detector array

After the magnet, the most important element of HELIOS is the silicon-detector array. The array measures the energy, return distance, and flight time of the detected particles. The silicon-detector array is designed so that particles are detected close to the solenoid axis, ensuring that particle flight times are very close to their cyclotron period. The inner opening of the array must, however, be large enough to permit transmission of the beam to the target. In the currently implemented silicon-detector array, 24 position-sensitive detectors (PSDs) are mounted on a 16 mm square extruded aluminum rod with a 10 mm diameter central bore with six detectors on each side. The position-sensitive axis of the detectors is along the beam direction. A square detector array causes some loss in position resolution since the values of z will vary across the detector. This correction is negligible compared to a position resolution of about 1 mm, except for the shallowest orbits where it can cause broadening by somewhat more than 1 mm.

The prototype silicon-detector array utilizes silicon detectors that were used in a previous application [7]. Each detector is made from a 12 mm $\times$ 56 mm silicon wafer with an active area of 9 mm $\times$ 50.5 mm, and a thickness of 700 μm. Position sensitivity is achieved by resistive charge division. The detector performance was characterized at Western Michigan University with a radioactive ^{241}Am source as well as protons from the tandem Van de Graaff accelerator elastically scattered from carbon foils. The proton-scattering measurements were carried out at beam energies of 2, 3, 4, and 5 MeV. To determine the position resolution, a mask with eight 0.5 mm wide slits covered the detector during the in-beam measurements. The results of the proton-scattering measurements are summarized in Figs. 5–7. Fig. 5 shows a two-dimensional spectrum of proton energy versus detector position. Groups corresponding to alpha particles from the ^{241}Am source, protons scattered from ^{12}C, and from ^{16}O and ^{1}H from water present in the target, are apparent.

From detector to detector, the energy resolution for protons varies between 25 and 55 keV FWHM and is weakly dependent on incident particle energy. Fig. 6 shows a composite proton-energy spectrum including data from all beam energies, for the 30 mm slit position, near the center of the detector, corresponding to a laboratory angle of approximately 60°. Fig. 7 shows position

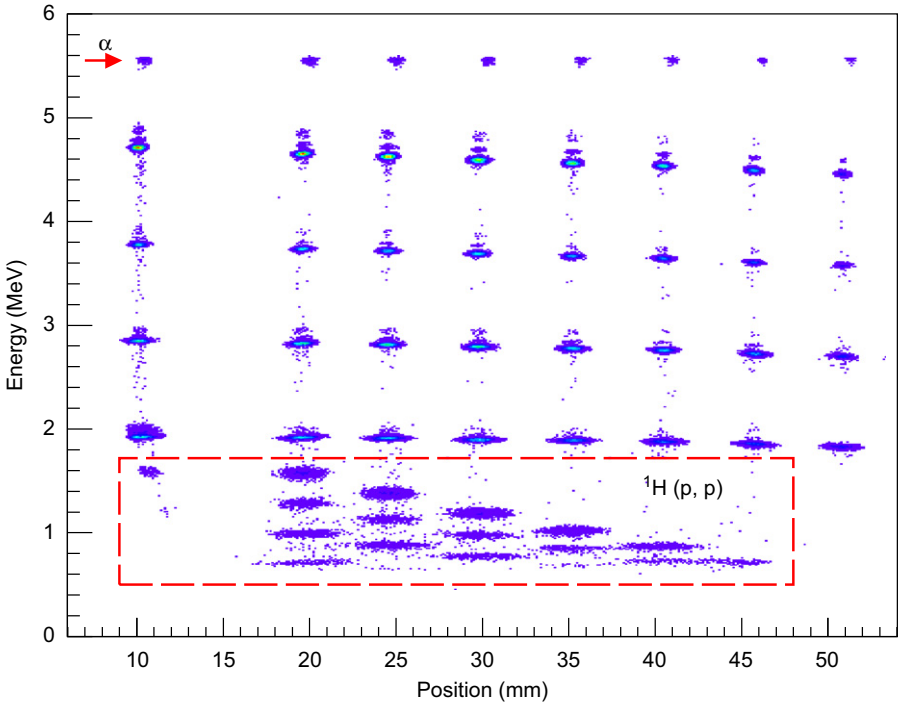

Fig. 5. Energy versus position spectrum for protons elastically scattered from a ^{12}C foil into an individual detector at four different beam energies. The detector was covered by a mask with 0.50 mm wide slits every 5 mm starting at 10 mm, with one omitted at 15 mm. Elastic scattering from ^{1}H, indicated by the box, and ^{16}O is also present due to water contamination in the target. The data at 5.5 MeV, indicated by the arrow, correspond to α particles from a ^{241}Am calibration source.

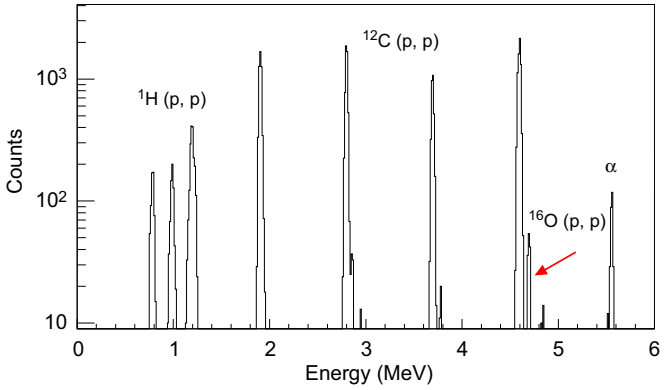

Fig. 6. Composite energy spectrum of protons scattered from ^{12}C, ^{16}O and ^{1}H, passing through the slit located at 30 mm, for bombarding energies of 2, 3, 4 and 5 MeV. The peak at 5.5 MeV corresponds to α particles from a ^{241}Am calibration source.

signals for protons scattered from ^{12}C at incident energies of 5 and 2 MeV. At 5 MeV, the resolution is comparable to the slit width of 0.5 mm, and at the lower energy it is 1.2 mm FWHM. These values satisfy the performance requirements of HELIOS.

Following the testing of each of the detectors, they were assembled into the silicon array. The 24 silicon detectors were mounted on four printed-circuit boards (PCBs), each board holding six detectors. These boards were assembled using a jig that permitted the detectors to be aligned with a precision of better than 200 μm. The electrical connection to the back contact of each detector was made by conductive epoxy, and this contact provides the total energy signal. The position contacts on either end of each silicon detector were made using aluminum wire bonds. The separation between the silicon detectors is 2.4 mm. Traces in the PCB carry the silicon-detector signals to two multi-pin connectors, and those signals are then carried on ribbon

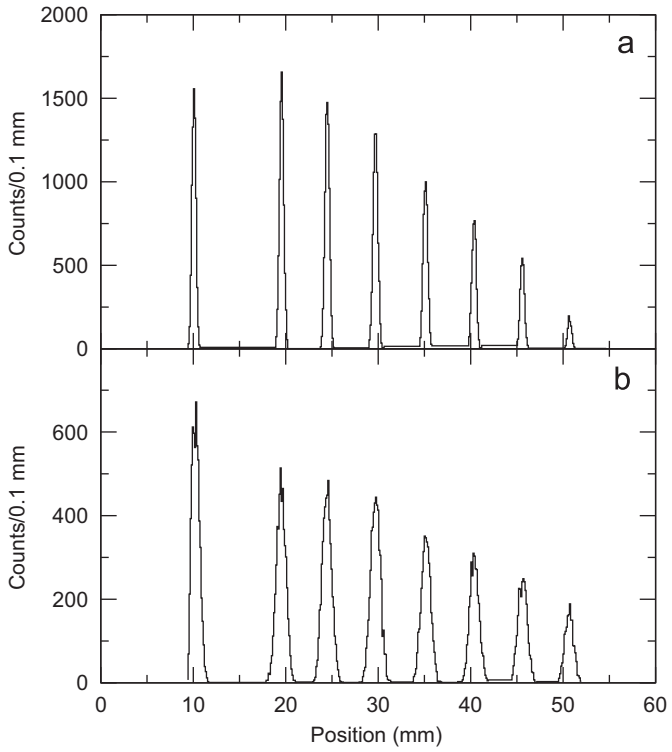

Fig. 7. Position spectra from p+^{12}C scattering at bombarding energies of (a) 5.0 MeV and (b) 2.0 MeV.

cables to a PCB feedthrough that takes them to the outside of the vacuum vessel. A photograph of one silicon detector affixed to a PCB is shown in Fig. 8.

Each of the PCBs was then epoxied to an aluminum bracket; these brackets were attached to the sides of the central aluminum

Fig. 8. Photograph of one silicon PSD mounted on a printed-circuit board as used in the HELIOS silicon-detector array.

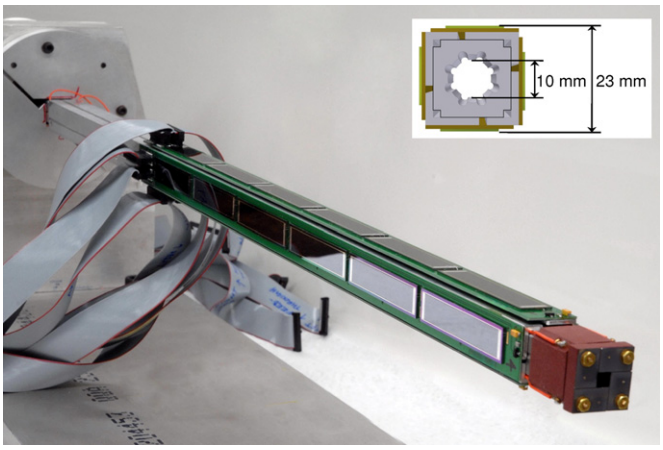

Fig. 9. The assembled HELIOS silicon-detector array held in its transport stand. The 5 mm × 5 mm four-element collimator can be seen at the end of the array. The inset shows a schematic drawing of the array cross-section.

tube. The assembled HELIOS detector array is shown in Fig. 9. As constructed, the array has a square cross-section 23 mm on a side and is 710 mm long with the active length covering 340 mm. The end of the array is fitted with a four-element, 5 mm × 5 mm square tantalum aperture for beam collimation; each element is insulated from the array and the beam current incident on each element can be monitored to aid beam tuning. The support for the silicon array includes a liquid-cooled copper block, providing cooling of the silicon detectors, although this cooling was not operational during the commissioning experiment. A linear bearing on the detector-array support structure permits axial translation of the array within the solenoid volume over a range of approximately 400 mm. To ensure good transmission of the beam through the array, it must be well aligned with respect to the beam axis. This alignment is achieved using a translation stage, providing motion perpendicular to the solenoid axis, and an alignment ring which allows the plane of the array to tilt.

Conventional electronics are used to process the silicon-detector signals. Each energy and position signal is first read out using a charge-sensitive preamplifier (Mesytec MSI-8p), and then fed to shaper/constant-fraction discriminator units (Mesytec MSCF-16) that provide trigger information, and produce analog signals that are digitized using conventional analog-to-digital converters. The main trigger for the silicon-array readout is formed from a logical OR of the discriminator outputs for all energy and position signals.

Target foils in HELIOS are mounted on a nine-position target fan, and the rotation angle is read out with a digital encoder. The distance between the target and the array can be changed by moving the target fan parallel to the beam axis, and the distance is measured with a laser range finder. Both the rotation and linear translation of the target fan can be accomplished under vacuum. In addition to target foils, the target fan can also hold a calibration source, a Faraday cup, and a silicon-detector telescope for beam diagnostics.

3.3. The acceptance

HELIOS disperses charged particles along the detector array in proportion to the reciprocal of their laboratory velocities, parallel to the beam, $v_{\parallel} = v_0\cos(\theta_{cm}) + V_{cm}$. Each detector thus subtends the same range of $\cos(\theta_{cm})$. The actual range of angles covered in the center-of-mass frame depends on the position of the array. As seen from Fig. 2, a range of center-of-mass angles from 21° to 42° is covered for the ground-state transition in the d(^{28}Si,p)^{29}Si reaction, given a field of 2.0 T, for the interval covered by the silicon array between −680 and −340 mm from the target.

The solid-angle acceptance also depends on the magnetic field and the reaction being studied. An increase in the magnetic field decreases the dispersion and thus increases the coverage in center-of-mass angles for a given detector position. For example, for the ground-state transition in the d(^{28}Si,p)^{29}Si reaction at 6 MeV/u with a central magnetic field of 2.0 T, each detector covers an interval of $\Delta\cos(\theta_{cm}) = 0.028$ and covers an azimuthal range of $\Delta\phi = 0.24\pi$, giving a solid angle of 0.021 sr per element, and a total solid angle coverage of 0.50 sr for the silicon array in the center-of-mass frame.

4. Simulations

Monte-Carlo simulations were performed to characterize the HELIOS response for the d(^{28}Si,p)^{29}Si reaction used for the commissioning of the instrument. These simulations are similar to those described in Ref. [5], but incorporate tracking of particles through the actual measured field map of the HELIOS solenoid, and a detector array with dimensions of the actual array. The target is a deuterated polyethylene [$(C_2D_4)_n$] foil with an areal density of 84 μg/cm^2, and all of the silicon detectors are assumed to have an intrinsic energy resolution of 50 keV FWHM. These parameters were chosen to match those of the commissioning experiment described below. Particles in these simulations were emitted uniformly in laboratory angle.

Fig. 10 shows a simulated spectrum of proton energy versus position for several different final states in ^{29}Si populated in the d(^{28}Si,p)^{29}Si reaction. The figure contains simulated events for three different target-detector separations, −95, −340, and −490 mm, as measured from the target to the most forward edge of the active silicon. The active array regions for these three separations are indicated by the sets of lines I, II, and III, respectively, in Fig. 10. The dashed curve shows the acceptance limit imposed by the size of the front of the silicon-detector array. The gaps in the spectrum that line up for different states at the same value of z are due to the spaces between individual detectors on the array. The combination of analytical calculation and Monte-Carlo simulation provides a convenient means to set up the spectrometer to study particular nuclear reactions.

5. The d(^{28}Si,p)^{29}Si measurement

5.1. Experimental setup

HELIOS was commissioned with a study of the inverse-kinematic reaction d(^{28}Si,p)^{29}Si. The (d,p) reaction on ^{28}Si is well-studied [1] and eight states in ^{29}Si are strongly populated between E_x=0 and 7 MeV, separated by an average interval of 0.91 MeV. Near 6 MeV there is a pair of states separated

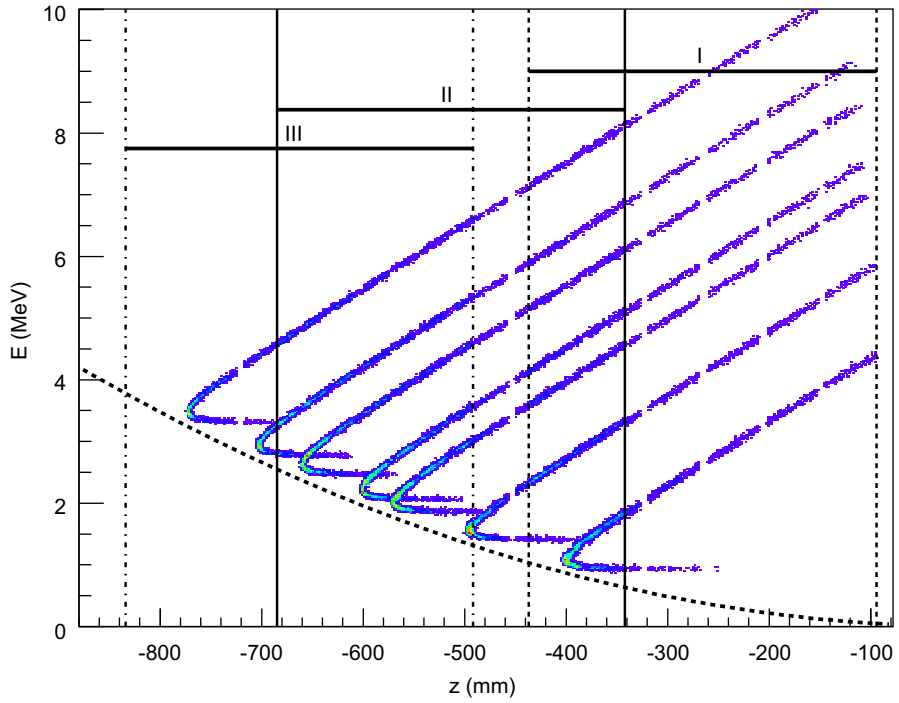

Fig. 10. Simulated energy versus position spectrum for seven states in ^{29}Si from the d(^{28}Si, p)^{29}Si reaction using the field map of the actual HELIOS solenoid. Pairs of vertical lines indicate the length of the array coverage with leading edges at −95, −340, and −490 mm. The particles that are intercepted by the front of the detector array determine a low-energy cutoff that is indicated by the dashed line.

by 190 keV. An experimental separation of these two states would demonstrate the Q-value resolution achievable with this device.

The measurement was carried out using the Argonne Tandem Linear Accelerator System (ATLAS) at Argonne National Laboratory. A ^{28}Si beam with energy 6 MeV/u bombarded an 84 μg/cm^2 target of deuterated polyethylene [$(C_2D_4)_n$] with an average beam current of 25 ppA. The magnetic field of the solenoid was set to a central value of 2.0 T.

The leading edge of the active region of the detector array was positioned at $z=-250$ mm with respect to the center of the magnet. The detector array remained in this position throughout the experiment. To cover different center-of-mass angle ranges, the target was placed at three different positions: 95, 340, and 490 mm away from the forward-most active element of the detector array. For the ground-state transition in ^{28}Si(d,p), these three positions covered the center-of-mass angle ranges of 37–53°, 21–42°, and 2–35°. The total axial range covered by the measurement was 740 mm, corresponding to center-of-mass angle range of 51° for the ground-state transition.

5.2. Results

Particle identification was achieved by measuring the flight time of the emitted particles relative to the 82 ns RF period of the ATLAS beam. Fig. 11 shows a representative time-of-flight spectrum from the experiment, which has two main features. The larger peak near 33 ns corresponds to protons that intercept the detector array at the end of one cyclotron orbit. The smaller peak in the timing spectrum near 66 ns corresponds to protons executing two cyclotron orbits and to particles with a mass-to-charge ratio of $A/q=2$ (α particles and deuterons). The total time resolution of the silicon array, including all silicon detectors was 9.1 ns FWHM, sufficient to isolate the reaction products of interest.

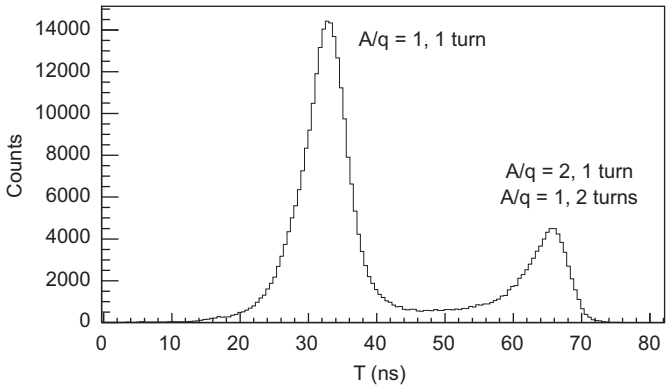

Fig. 11. Time-of-flight spectrum for protons emitted from ^{28}Si+$(C_2D_4)_n$ collisions. The peak near 33 ns corresponds to protons completing one cyclotron orbit. The peak near 66 ns corresponds to protons completing two cyclotron orbits as well as to particles with $A/q=2$.

Fig. 12 shows the measured relationship between the energy and return distance z of particles detected in the silicon array, for data taken with the target-to-detector separation of $\Delta z=340$ mm. The events are required to have a flight time consistent with protons executing single cyclotron orbits. The six vertical bands of counts correspond to the six silicon-detector positions within the array. The diagonal ridges in the data correspond to the kinematic loci for transitions to different excited states in ^{29}Si. The solid vertical lines indicate the outer limits to the active region of the whole silicon-detector array. The thick dashed lines show the cuts in acceptance from (A) the size of the silicon-detector array and (B) the geometry of the target frame which, for this particular setting, only allowed particles to be emitted with angles greater than 114° relative to the solenoid axis. That obstruction was corrected for data obtained at the other target-position settings. For some detectors, there is a depletion of counts in the center of

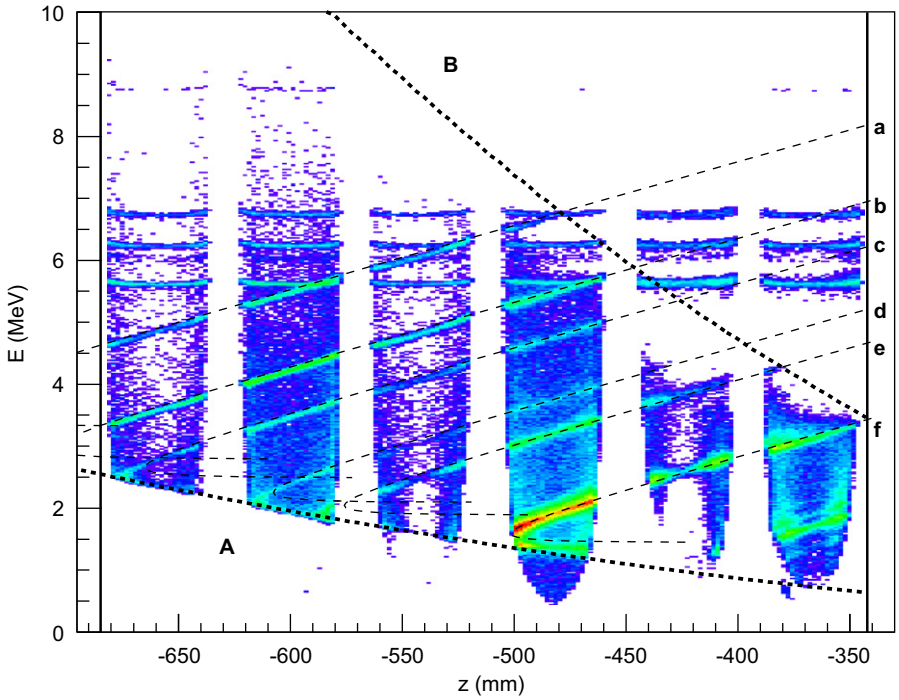

Fig. 12. Energy-versus-position spectrum for a target-to-detector separation of $\Delta z = 340$ mm, for events with flight times consistent with single proton orbits. The thin dashed black lines labeled a, b, c, d, e, and f indicate the analytically calculated position of the kinematic groups with excitation energies of 0.00, 1.27, 2.03, 3.07, 3.62, and 4.90 MeV, respectively. The thick dashed curves are the acceptance cutoffs discussed in the text. The pair of vertical lines indicate the range of the array coverage for this setting.

the detector; this arises from high detector thresholds made necessary by large electronic noise in this first commissioning experiment. Additional shielding of the detector cables has since eliminated this problem. The thin dashed lines through the diagonal ridges in the data represent the results of the analytical calculations shown in Fig. 2(a). The agreement between the data and these calculations is excellent.

The backgrounds in Fig. 12 arise from two sources. The groups of counts at constant energies as a function of z correspond to alpha particles from a ^{228}Th calibration source. These particles are in random time correlation with the beam and cannot be completely eliminated using a time-of-flight selection. The smooth background throughout the plot arises from protons emitted from fusion-evaporation reactions of ^{28}Si+^{12}C in the target, which have the same time of flight as those from the reaction of interest, and hence can also not be eliminated without coincidence identification of the recoiling ^{29}Si ion. Recoil detection was not implemented in this commissioning experiment, however, it has since been employed for other studies [6]. Fig. 13 shows a composite figure containing events from all three target positions. The gap in the data for proton energies greater than 4 MeV near $z = -380$ mm is produced by the obstruction of the target frame discussed above.

Only a small fraction of protons can execute two cyclotron orbits without first intercepting the silicon-detector array. Fig. 14 shows the energy-versus-position spectrum with flight times corresponding to two orbits for the setting with the largest target-to-detector separation, $\Delta z = 490$ mm. Despite the lower statistics, diagonal ridges are still present with a slope that is half that of the single-turn data, representing transitions to states in ^{29}Si. Although the acceptance for such events is limited, it is possible to extend the center-of-mass angle range through the use of multi-turn orbits in certain situations.

The transformation of quantities measured in the laboratory to physical quantities in the center-of-mass system is straightforward. To determine the excitation energy in ^{29}Si, the data in the energy-versus-position matrices are corrected for the common, known slope, yielding the particle energy in the center-of-mass system and the excitation energy. The resulting excitation-energy spectrum for a single silicon detector centered at 411 mm with the leading edge of the array at $\Delta z = 95$ mm appears in Fig. 15(a). A smooth background has been subtracted from these data. The excitation-energy resolution here is approximately 80 keV FWHM, and the two states at 6.19 and 6.38 MeV are resolved. Fig. 15(b) shows a similar spectrum for the entire array at the same target-to-detector separation, and Fig. 15(c) shows a composite spectrum including all events from the three target positions. The resolution degrades slightly due to the inclusion of silicon detectors with slightly worse intrinsic resolution, and the corresponding values for the resolution are 100, and 130 keV FWHM, for the spectra in Fig. 15(b) and (c), respectively. Also shown in Fig. 15(c) is the unsubtracted composite excitation-energy spectrum.

To obtain the center-of-mass scattering angle, the excitation energy is first determined using the correlation between laboratory energy and position of the detected light particle. Then, the cosine of the center-of-mass angle is given by

$$\cos(\theta_{cm}) = \frac{v_{lab}^2 - V_{cm}^2 - v_0^2}{2 v_0 V_{cm}}. \quad (4)$$

Here v_{lab} is the laboratory velocity of the detected particle in the laboratory frame determined from the measured energy. V_{cm} is the velocity of the center-of-mass system fixed by the bombarding energy, and v_0 is the particle velocity in the center-of-mass frame, determined from the bombarding energy, the excitation energy and the ground-state Q-value. With the excitation energy fixed, the center-of-mass angle is determined by E_{lab}.

In this commissioning measurement the detection efficiencies for states at higher excitation energy were limited by threshold effects because of lower proton energies. The proton energies

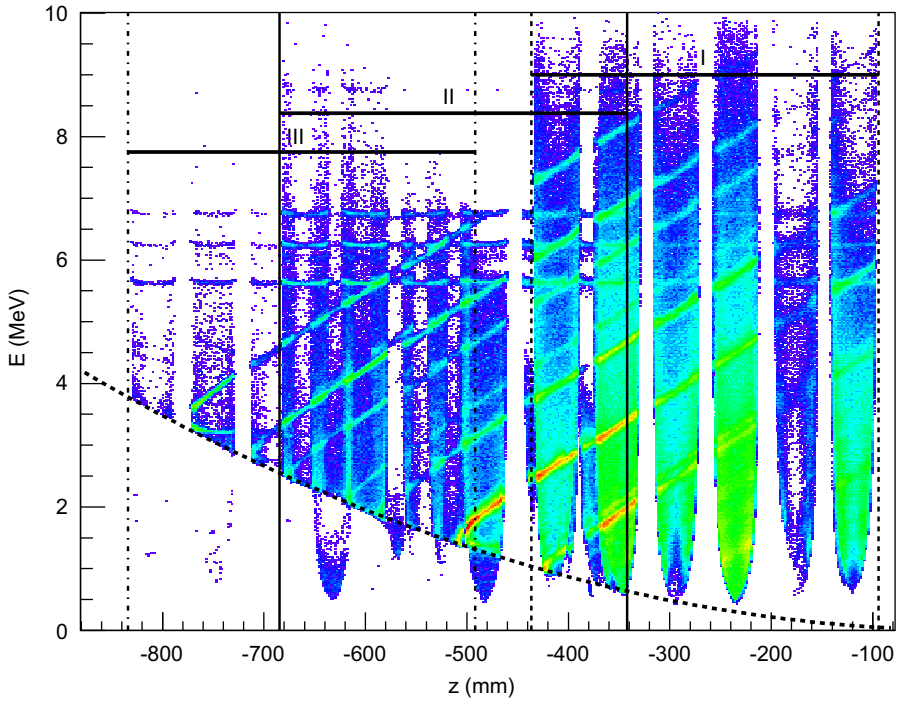

Fig. 13. Composite energy-versus-position spectrum for protons, including events for all target-silicon-array separations. Pairs of vertical lines indicate the length of the array coverage, for the settings with the leading edge of the detector array at (I) −95 mm, (II) −340 mm, and (III) −490 mm. The thick dashed curve represents the acceptance cutoff described in the text.

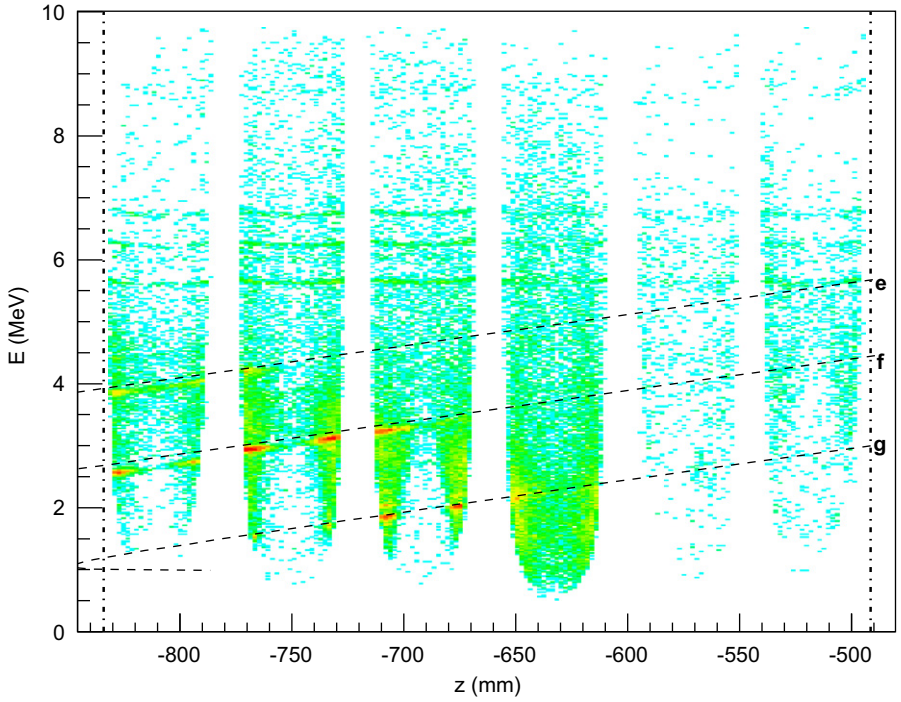

Fig. 14. Energy-versus-position spectrum at $\Delta z = 490$ mm, for events with flight times consistent with two proton cyclotron orbits. The dashed lines represent the analytically calculated energy-position correlations for kinematic groups with excitation energies of (e) 3.62 MeV, (f) 4.90 MeV, and (g) 6.38 MeV (same labeling as Fig. 14).

from the ground and first-excited-state transitions were large enough so that the effects were negligible. For these states the relative detector efficiencies were normalized to the α spectrum of the ^{228}Th calibration source. Fig. 16 shows angular distributions extracted for these two transitions using data from the $\Delta z = 490$ mm position setting. Each point includes data from approximately half of one silicon detector. Center-of-mass angles forward of 10° correspond to protons with very shallow trajectories that are detected before completing their full cyclotron orbit as discussed above; the solid-angle acceptance for these orbits is very sensitive to the relative alignment of the silicon array and we omit those data from Fig. 16. In this commissioning experiment, the beam current was not measured, and so the cross-section scale is arbitrary.

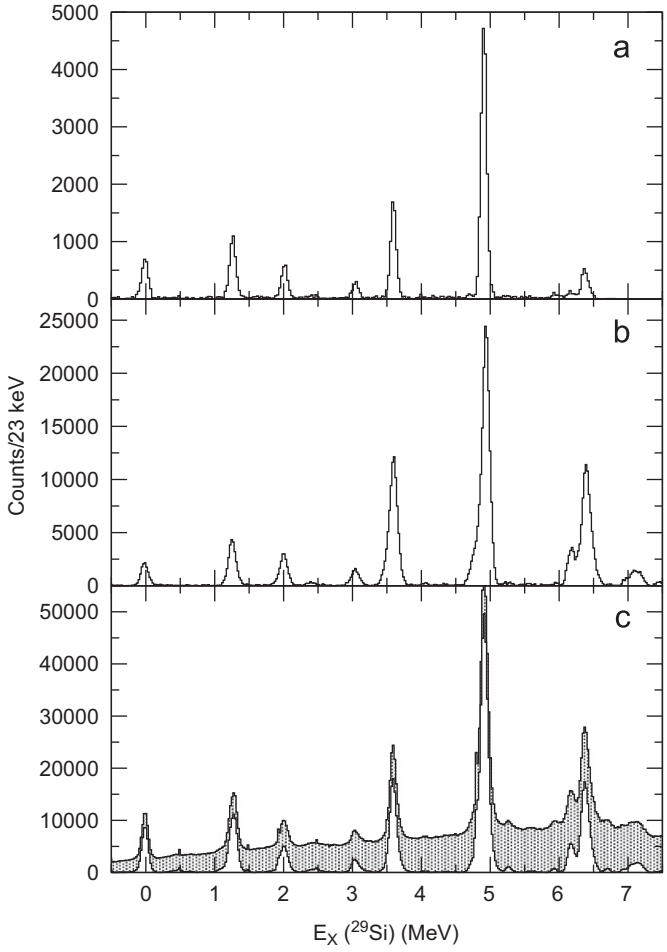

Fig. 15. Excitation-energy spectra for d(^{28}Si,p)^{29}Si reaction. (a) Spectrum for a single detector subtending 386–437 mm from the target (furthest detector position from the target with the leading edge of the array 95 mm from the target). (b) Spectrum for the entire array at the same target-position setting, $\Delta z = 95$ mm. (c) Composite spectrum for all detectors including events from three position settings. In each case a smooth background has been subtracted from the spectrum. The shaded histogram in (c) shows the composite spectrum before background subtraction.

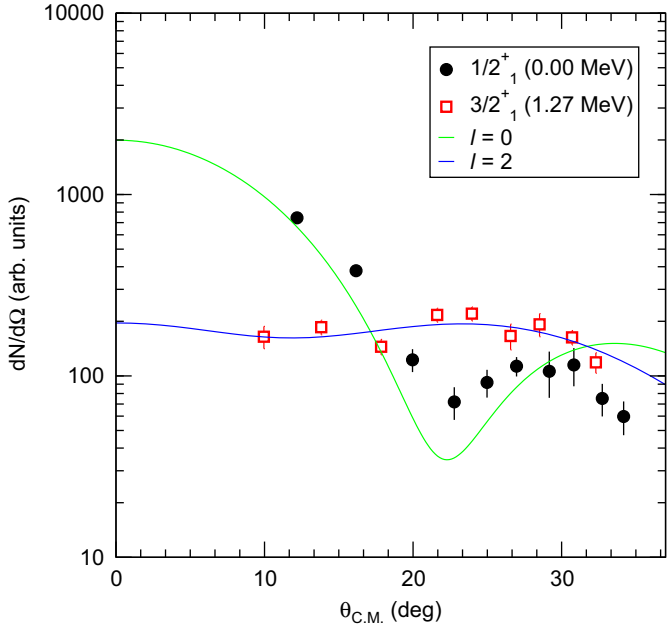

Fig. 16. Proton angular distributions for transitions to the ground and first-excited states of ^{29}Si. The curves correspond to distorted-wave Born approximation calculations for this reaction at a deuteron bombarding energy of 12 MeV using optical-model parameters from Ref. [1].

The angular distribution for the $\frac{1}{2}^+$ ground state shows a shape characteristic of an angular momentum transfer of $\ell = 0$, with a strong maximum near $\theta_{cm} = 0^\circ$, and minimum near $\theta_{cm} = 22^\circ$. The angular distribution for the $\frac{3}{2}^+$ first-excited state shows a much weaker dependence on scattering angle, as expected for an $\ell = 2$ transition. The shapes of these angular distributions are similar to those observed by Mermaz et al. [1] in normal kinematics at a deuteron bombarding energy of 18 MeV. The relative cross-sections for the ground- and first-excited-state transitions agree well with those obtained by Mermaz et al. Similar measurements with HELIOS have been used recently to determine the spins of excited states in ^{13}B populated in the ^{12}B(d,p)^{13}B reaction in inverse kinematics [6].

6. Conclusions

We have commissioned HELIOS using the neutron-transfer reaction d(^{28}Si,p)^{29}Si reaction at 6.0 MeV/u. The results of the measurement validated the concept and showed that the resolution, acceptance, and transport properties of the device were consistent with expectations of both the analytical calculations and the Monte-Carlo simulations of the response of the spectrometer. In particular, the technique of particle identification for low-energy protons was demonstrated, and a Q-value resolution of 80 keV was achieved. These results represent a significant improvement over those achievable with other detector approaches [8–11]. The large acceptance of the device permitted detection of particles over a large range of center-of-mass angles with large solid-angle coverage. Since this commissioning run, further experiments have utilized the properties of HELIOS to, for example, determine spin assignments for narrowly spaced states in ^{13}B populated with the (d,p) reaction in inverse kinematics with a radioactive ^{12}B beam [6]. Several other studies have been carried out with HELIOS using both stable and unstable beams with masses ranging from $A = 11$ to 136.

While these results are very encouraging, the present implementation of HELIOS is still that of a demonstration prototype. A number of improvements to the apparatus are planned, including new silicon detectors in an arrangement that will provide twice the solid-angle coverage and improved overall resolution as well as greater center-of-mass-angle acceptance. Also, we plan for the addition of a gas parallel-plate avalanche counter and ionization chamber for the detection and identification of recoiling heavy nuclei that cannot be so identified using silicon ΔE–E techniques. While the present spectrometer configuration is tailored to the detection of particles emitted with laboratory angles greater than 90°, the advantages of simplified kinematics and improved resolution also apply to reactions in inverse kinematics that emit light-charged particles forward of 90°, such as (d,^{3}He). Work is currently underway to accommodate such reactions. With these features in mind, we believe that HELIOS represents a powerful new tool for the study of nuclear reactions in inverse kinematics.

Acknowledgments

This work was supported by the U.S. Department of Energy, Office of Nuclear Physics, under Contracts DE-FG02-04ER41320 and DE-AC02-06CH11357.

References

[1] M.C. Mermaz, C.A. Whitten, J.W. Champlin, A.J. Howard, D.A. Bromley, Phys. Rev. C 4 (1971) 1778 URL: 〈http://link.aps.org/doi/10.1103/PhysRevC.4.1778〉.

[2] J.S. Winfield, W.N. Catford, N.A. Orr, Nucl. Instr. and Meth. A 396 (1997) 147 URL: 〈http://dx.doi.org/10.1016/S0168-9002(97)00752-3〉..

[3] J.P. Schiffer, in: I.Y. Lee (Ed.), Proceedings of the Workshop on Experimental Equipment for an Advanced ISOL Facility, Lawrence Berkeley National Laboratory, 1998, LBNL-42138, pp. 667–678.

[4] A.H. Wuosmaa, T. Al Tahtamouni, J.P. Schiffer, Nucl. Phys. A 746 (2004) 267 URL: 〈http://dx.doi.org/10.1016/j.nuclphysa.2004.09.039〉.

[5] A.H. Wuosmaa, J.P. Schiffer, B.B. Back, C.J. Lister, K.E. Rehm, Nucl. Instr. and Meth. A 580 (2007) 1290 URL: 〈http://dx.doi.org/10.1016/j.nima.2007.07.029〉.

[6] B.B. Back, S.I. Baker, B.A. Brown, C.M. Deibel, S.J. Freeman, B.J. DiGiovine, C.R. Hoffman, B.P. Kay, H.Y. Lee, J.C. Lighthall, et al., Phys. Rev. Lett. 104 (2010) 132501 URL: 〈http://prl.aps.org/pdf/PRL/v104/i13/e132501〉.

[7] D.J. Blumenthal, Ph.D. Thesis, Yale University, 1994.

[8] C. Demonchy, W. Mittig, H. Savajols, P. Roussel-Chomaz, M. Chartier, B. Jurado, L. Giot, D. Cortina-Gil, M. Caamaño, G. Ter-Arkopian, et al., Nucl. Instr. and Meth. A 573 (2007) 145 URL: 〈http://dx.doi.org/10.1016/j.nima.2006.11.025〉.

[9] E. Pollacco, D. Beaumel, P. Roussel-Chomaz, E. Atkin, P. Baron, J.P. Baronick, E. Becheva, Y. Blumenfeld, A. Boujrad, A. Drouart, et al., Eur. Phys. J. A 25 (2005) 287 URL: 〈http://www.springerlink.com/content/U21376655505 5235〉.

[10] W.N. Catford, C.N. Timis, R.C. Lemmon, M. Labiche, N.A. Orr, L. Caballero, R. Chapman, M. Freer, M. Chartier, H. Savajols, et al., J. Phys. G 31 (2005) S1655 URL: 〈http://stacks.iop.org/0954-3899/31/i=10/a=049〉.

[11] S. Pain, J. Cizewski, R. Hatarik, K. Jones, J. Thomas, D. Bardayan, J. Blackmon, C. Nesaraja, M. Smith, R. Kozub, et al., Nucl. Instr. and Meth. B 261 (2007) 1122 URL: 〈http://dx.doi.org/10.1016/j.nimb.2007.04.289〉.